Electronic Supplementary Material (ESI) for Journal of Materials Chemistry A.

Supporting information

H_2-production and electron-transfer mechanism of noble-metal-free WO_3@$ZnIn_2S_4$ S-scheme heterojunction photocatalyst

Shuang Cao,[a] *Jiaguo Yu,*[a,b] *Swelm Wageh,*[c,*] *Ahmed A. Al-Ghamdi,*[c] *Mitra Mousavi,*[d] *Jahan B. Ghasemi*[d] *and Feiyan Xu*[b,*]

[a] State Key Laboratory of Advanced Technology for Materials Synthesis and Processing, Wuhan University of Technology, Luoshi Road 122, Wuhan, 430070, P.R. China

[b] Laboratory of Solar Fuel, Faculty of Materials Science and Chemistry, China University of Geosciences, Lumo Road 388, Wuhan, 430074, P. R. China

[c] Department of Physics, Faculty of Science, King Abdulaziz University, Jeddah 21589, Saudi Arabia

[d] School of Chemistry, College of Science, University of Tehran, P.O. Box 14155-6455, Tehran, Iran

* E-mail: xufeiyan@cug.edu.cn; wswelm@kau.edu.sa

1. Experimental section

1.1 Chemicals

Tungsten hexachloride (WCl_6), Indium chloride ($InCl_3{\cdot}xH_2O$), 5,5-Dimethyl-1-pyrroline N-oxide (DMPO) were purchased from Macklin Reagent Co., Ltd. Polyacrylonitrile (PAN, M_W =150,000), thioacetamide (TAA), N, N-Dimethylformamide (DMF), zinc chloride and ethanol were purchased from Sinopharm Chemical Reagent Co., Ltd. All the reagents were analytical grade and used without further purification.

1.2 Characterizations

Field emission scanning electron microscope (FESEM) and transmission electron microscopy (TEM) images were observed on JSM 7500F and Talos F200S, respectively. X-Ray diffraction (XRD) patterns were performed on a Shimadzu X-ray diffractometer (XRD-6100, Japan) with Cu *K*α radiation. UV-visible diffuse reflectance spectra (DRS) were obtained on a Shimadzu UV-2600 UV–visible spectrophotometer (Japan). The Brunauer-Emmett-Teller (BET) specific surface area (S_{BET}) and pore size distribution of the powders were obtained by nitrogen adsorption in a nitrogen adsorption apparatus (TriStar II 3020, Micromeritics, USA). X-ray photoelectron spectroscopy (XPS) was performed on a Thermo ESCALAB 210 XPS spectrometer system (UK) with Al *K*α radiation. *In-situ* XPS measurements were conducted under the same condition except that light irradiation was introduced. Time-resolved photoluminescence (TRPL) spectra

was recorded on a fluorescence lifetime spectrophotometer (FLS 1000, Edinburgh, UK) at an excitation wavelength of 325 nm. The average decay time (τ_a) was calculated from the following formula:

$$\tau_a = \frac{A_1\tau_1{}^2 + A_2\tau_2{}^2 + A_3\tau_3{}^2}{A_1\tau_1 + A_2\tau_2 + A_3\tau_3} \quad (1)$$

Electrochemical measurements were conducted using an electrochemical analyzer (CHI660C Instruments, Shanghai) in a standard three-electrode system. Pt wire, Ag/AgCl (saturating KCl) and 0.5 M Na_2SO_4 solution functioned as the counter electrode, reference electrode and electrolyte, respectively. For the working electrode, 20 mg of photocatalysts were dispersed in 1.0 mL of ethanol and 10 μL of Nafion solution to make slurry, which was then coated onto F-doped SnO_2-coated (FTO) glass electrode with an exposed area of *ca.* 1 cm^2. Afterward, the electrode was dried in an oven at 60 °C for 1 h.

1.3 Apparent quantum yield (AQY) calculation

The apparent quantum yield (AQY) was measured under the same photocatalytic reaction conditions except using monochromatic light of 420 nm as the light source. The light intensity was measured as 3 mW/cm^2 and the irradiation area was determined to be 1cm^2. The number of incident photons and the AQY were calculated according to the following equations:

$$N = \frac{E\lambda}{hc} = \frac{3 \times 10^{-3} \times 8.5 \times 3600 \times 420 \times 10^{-9}}{6.626^{-34} \times 3 \times 10^8} = 1.94 \times 10^{20}$$

(2)

$$AQY = \frac{2 \times the\ number\ of\ evolved\ H_2}{the\ number\ of\ incident\ photons} \times 100 = \frac{2 \times 3.5 \times 10^{23} \times 10 \times 10^{-6}}{1.94 \times 10^{20}} \times 100 = 3.61\%$$

(3)

1.4 Band structure (E_g, E_C and E_V) calculation

The band structure (E_{CBM}, E_{VBM} and E_g) of WO_3 and $ZnIn_2S_4$ was calculated according to the following empirical formulas:

$$\alpha h\nu = A(h\nu - E_g)^{n/2} \quad (4)$$

$$E_{VBM} = E_{FP} + E_{cuttoff} \quad (5)$$

$$E_{CBM} = E_g - E_{VBM} \quad (6)$$

where α, E_g, and $h\nu$ represent the absorption index, energy gap and photon energy, respectively. As for n, different types of semiconductors have different n values. The n values of indirect band gap semiconductors and direct band gap semiconductors are 4 and 1, respectively. E_{FP} represents the flat band potential while E_{cutoff} stands for the cutoff edge obtained from VB XPS spectra.

2. Supporting Figures

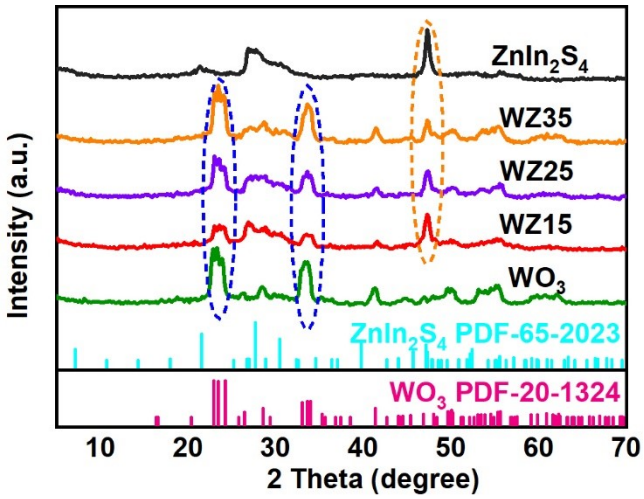

Fig. S1 XRD patterns of WO_3, $ZnIn_2S_4$ and WZ*x*. WZ*x* represents the WO_3@$ZnIn_2S_4$ composite, where W and Z represent WO_3 and $ZnIn_2S_4$, respectively; *x* indicates the molar percentage of WO_3 with respect to $ZnIn_2S_4$.

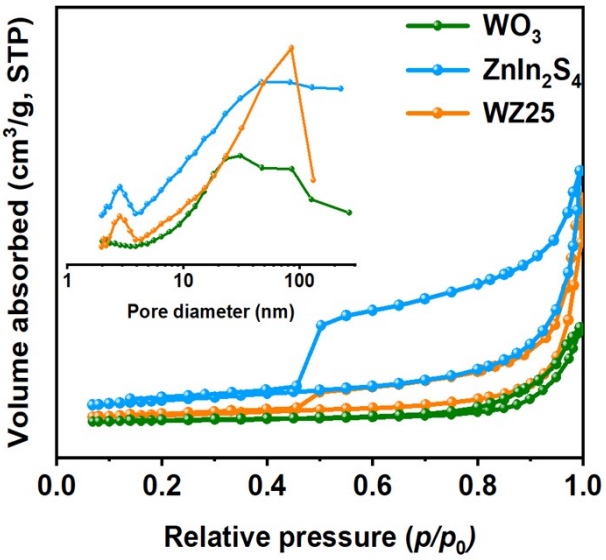

Fig. S2 Nitrogen adsorption-desorption isotherms and the corresponding pore size distribution (inset) of WO_3, $ZnIn_2S_4$ and WZ25. WZ25 represents the WO_3@$ZnIn_2S_4$ composite, where W and Z represent WO_3 and $ZnIn_2S_4$, respectively; *25* indicates the molar percentage of WO_3 with respect to $ZnIn_2S_4$.

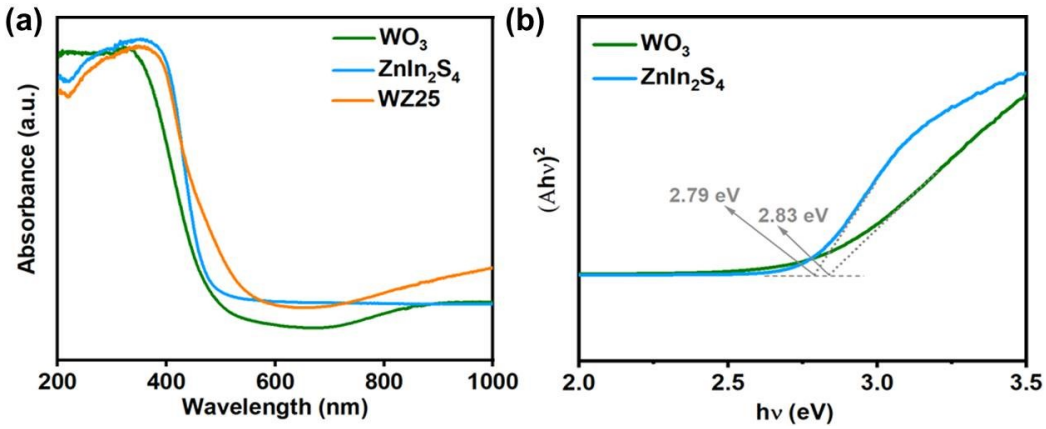

Fig. S3 (a) UV-vis spectra of WO_3, $ZnIn_2S_4$ and WZ25, (b) Kubelka-Monk plots of WO_3 and $ZnIn_2S_4$. WZ25 represents the WO_3@$ZnIn_2S_4$ composite, where W and Z represent WO_3 and $ZnIn_2S_4$, respectively; *25* indicates the molar percentage of WO_3 with respect to $ZnIn_2S_4$.

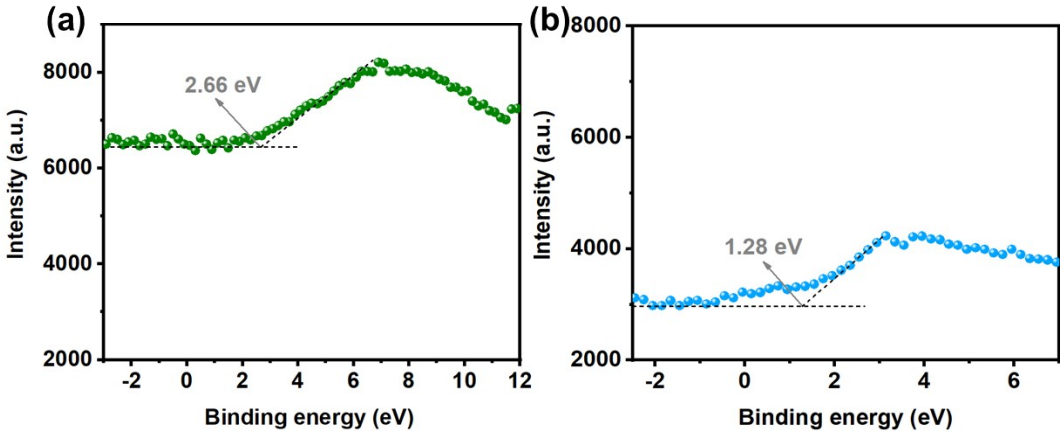

Fig. S4 Valence band XPS spectra of (a) WO_3 and (b) $ZnIn_2S_4$.

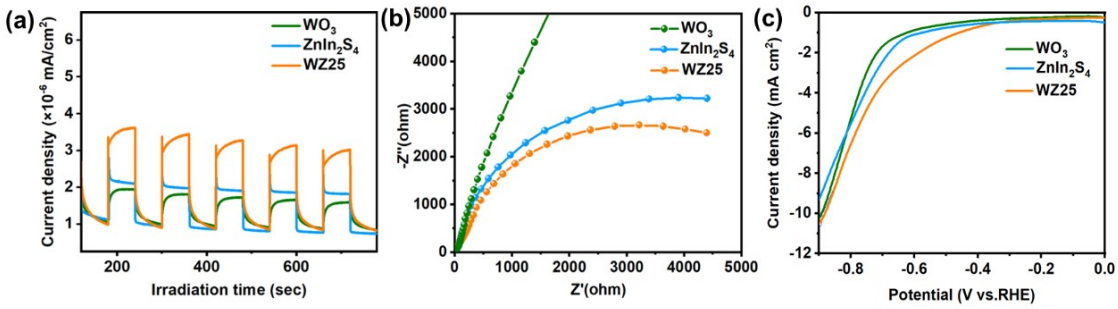

Fig. S5 (a) Transient photocurrent response, (b) Nyquist plots and (c) polarization curves of WO_3, $ZnIn_2S_4$ and WZ25. WZ25 represents the WO_3@$ZnIn_2S_4$ composite, where W and Z represent WO_3 and $ZnIn_2S_4$, respectively; *25* is the molar percentages of WO_3 with respect to $ZnIn_2S_4$.

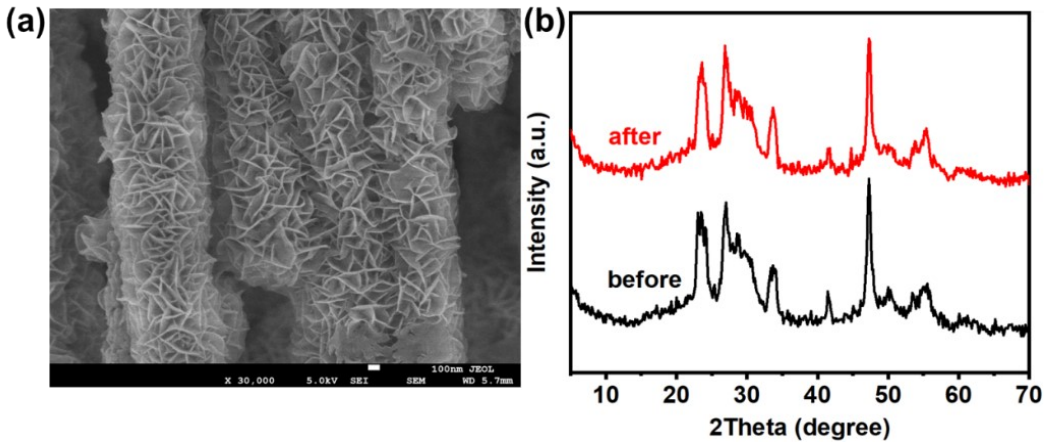

Fig. S6 (a) FESEM and (b) XRD pattern of WZ25 after cycle photocatalytic reactions. WZ25 represents the WO_3@$ZnIn_2S_4$ composite, where W and Z represent WO_3 and $ZnIn_2S_4$, respectively; *25* is the molar percentages of WO_3 with respect to $ZnIn_2S_4$.

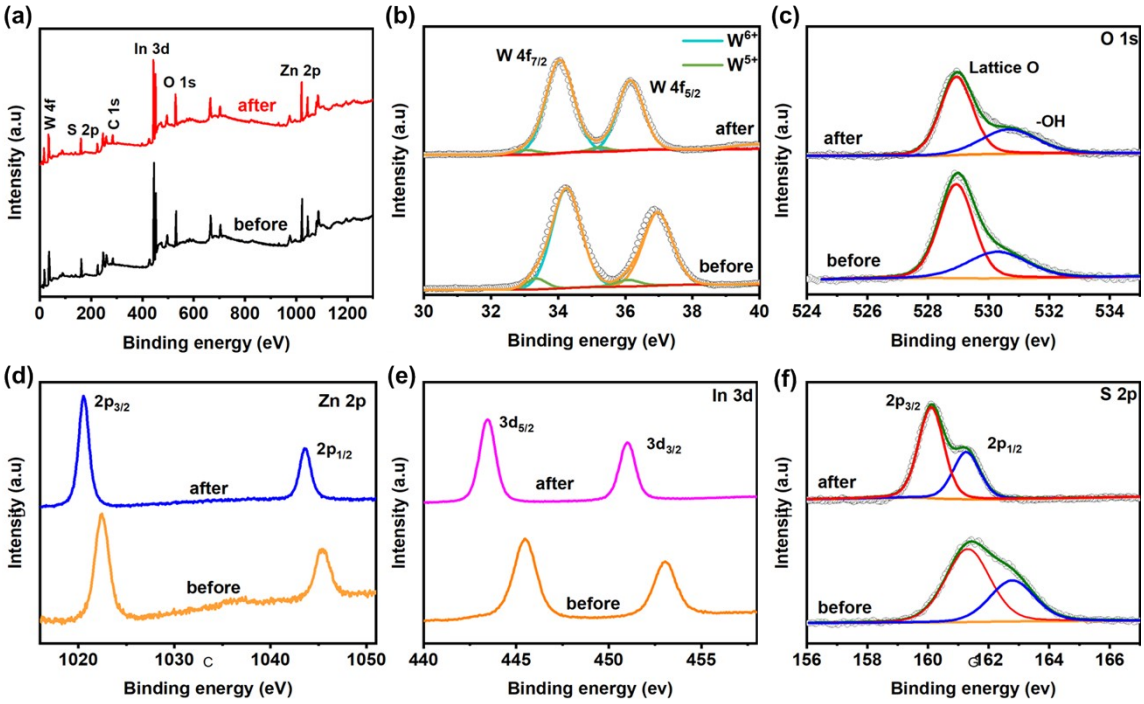

Fig. S7 (a) XPS survey spectra, XPS spectra of (b) W 4f and (c) O 1s, (d) Zn 2p, (e) In 3d and (f) S 2p of WZ25 before and after cycled photocatalytic reactions. WZ25 represents the WO_3@$ZnIn_2S_4$ composite, where W and Z represent WO_3 and $ZnIn_2S_4$, respectively; *25* is the molar percentages of WO_3 with respect to $ZnIn_2S_4$.

3. Supporting Tables

Table S1. Physical properties of WO_3, $ZnIn_2S_4$ and WZ25.

Samples	S_{BET} ($m^2\ g^{-1}$)	d_{pore} (nm)	V_{pore} ($cm^3\ g^{-1}$)
WO_3	9	17	0.04
$ZnIn_2S_4$	36	10	0.09
WZ25	17	12	0.05

Table S2. The fitted lifetimes obtained from decay curves of WO_3 and WZ25 dispersed in DMF under argon atmosphere. WZ25 represents the WO_3@$ZnIn_2S_4$ composite, where W and Z represent WO_3 and $ZnIn_2S_4$, respectively; 25 is the molar percentages of WO_3 with respect to $ZnIn_2S_4$.

Sample	τ_1 **(ns)**	τ_2 **(ns)**	τ_3 **(ns)**
WO_3	1.19	2.08	34.98
WZ25	0.91	2.05	24.53

Table S3. Comparison of photocatalytic H_2 generation performance of various photocatalysts with and without noble metal cocatalysts.

Catalyst	Cocatalyst	Hole scavenger	H_2 evolution rate ($\mu mol\ h^{-1}\ g^{-1}$)	Ref.
WO_3@$ZnIn_2S_4$	None	TEOA	8500	This
WO_3/g-C_3N_4	Pt	Lactic acid	982	[1]
g-C_3N_4/TiO_2/IrO_x	Pt	Methanol	8150	[2]
g-C_3N_4/Onion-like carbon	Pt	TEOA	3086	[3]
$CuInS_2$/$ZnIn_2S_4$	Pt	0.35 M NaS_2 and 0.25 M	3430	[4]
TiO_2/$ZnIn_2S_4$	Pd	TEOA	5350	[5]
Black phosphorus/Bi_2WO_6	Pt	TEOA	4208	[6]
Ta_3N_5/$BaTaO_2N$	Pt	methanol	182	[7]
Covalent triazine frameworks-Benzothiadiazole/Thio	Pt	TEOA	6608	[8]
SnO_2/UiO-66-NH_2	Pt	Trimethylamine	2167	[9]
SnO_2/g-C_3N_4	Au	Methanol	770	[10]
Multi-edged TiO_2	Ru	Methanol	7200	[11]

References

1 J.W. Fu, Q.L. Xu, J.X. Low, C.J. Jiang, J.G. Yu, Ultrathin 2D/2D WO_3/g-C_3N_4 step-scheme H_2-production photocatalyst, *Appl. Catal. B-Environ.*, 2019, **243**, 556-565.

2 H.S. Moon, K.C. Hsiao, M.C. Wu, Y. Yun, Y.J. Hsu, K. Yong, Spatial Separation of Cocatalysts on Z-Scheme Organic/Inorganic Heterostructure Hollow Spheres for Enhanced Photocatalytic H_2 Evolution and In-Depth Analysis of the Charge-Transfer Mechanism, *Adv. Mater.*, 2022, 2200172.

3 Y. Shi, Q. Zhao, J. Li, G. Gao, J. Zhi, Onion-liked carbon-embedded graphitic carbon nitride for enhanced photocatalytic hydrogen evolution and dye degradation, *Appl. Catal. B-Environ.*, 2022, **308**, 121216.

4 Z. Guan, J. Pan, Q. Li, G. Li, J. Yang, Boosting Visible-Light Photocatalytic Hydrogen Evolution with an Efficient $CuInS_2$/$ZnIn_2S_4$ 2D/2D Heterojunction, *ACS Sustain. Chem. Eng.*, 2019, **7**, 7736-7742.

5 P. She, J.S. Qin, J. Sheng, Y. Qi, H. Rui, W. Zhang, X. Ge, G. Lu, X. Song, H. Rao, Dual-Functional Photocatalysis for Cooperative Hydrogen Evolution and Benzylamine Oxidation Coupling over Sandwiched-Like Pd@TiO_2@$ZnIn_2S_4$ Nanobox, *Small*, 2022, **18**, 2105114.

6 J. Hu, D. Chen, Z. Mo, N. Li, Q. Xu, H. Li, J. He, H. Xu, J. Lu, Z-Scheme 2D/2D Heterojunction of Black Phosphorus/Monolayer Bi_2WO_6 Nanosheets with Enhanced Photocatalytic Activities, *Angew. Chem. Int. Edit.*, 2019, **58**, 2073-2077.

7 B. Dong, J. Cui, Y. Gao, Y. Qi, F. Zhang, C. Li, Heterostructure of 1D Ta_3N_5 Nanorod/$BaTaO_2$ N Nanoparticle Fabricated by a One-Step Ammonia Thermal Route for Remarkably Promoted Solar Hydrogen Production, *Adv. Mater.*, 2019, **31**, 1808185.

8 W. Huang, Q. He, Y. Hu, Y. Li, Molecular Heterostructures of Covalent Triazine Frameworks for Enhanced Photocatalytic Hydrogen Production, *Angew. Chem. Int. Edit.*, 2019, **58**, 8676-8680.

9 J. Sui, H. Liu, S. Hu, K. Sun, G. Wan, H. Zhou, X. Zheng, H.L. Jiang, A General Strategy to Immobilize Single-Atom Catalysts in Metal-Organic Frameworks for Enhanced Photocatalysis, *Adv. Mater.*, 2022, **34**, 2109203.

10 A. Zada, M. Humayun, F. Raziq, X. Zhang, Y. Qu, L. Bai, C. Qin, L. Jing, H. Fu, Exceptional Visible-Light-Driven Cocatalyst-Free Photocatalytic Activity of g-C_3N_4 by Well Designed Nanocomposites with Plasmonic Au and SnO_2, *Adv. Energy Mater.*, 2016, **6**, 1601190.

11 H.B. Zhang, S.W. Zuo, M. Qiu, S.B. Wang, Y.F. Zhang, J. Zhang, X.F.D. Luo, Direct probing of atomically dispersed Ru species over multi-edged TiO_2 for highly efficient photocatalytic hydrogen evolution, *Sci. Adv.*, 2020, **6**, eabb9823.